Carrier transport and photoconductive gain mechanisms of AlGaN MSM photodetectors with high Al Content

Zhicheng Dai (代志诚)[1], Yushen Liu (刘玉申)[2], Guofeng Yang (杨国锋)[1*], Feng Xie (谢峰)[3], Chun Zhu (朱纯)[1], Yan Gu (谷燕)[1], Naiyan Lu (陆乃彦)[1], Qigao Fan (樊启高)[1], Yu Ding (丁宇)[1], Yuhang Li (李宇航)[1], Yingzhou Yu (虞瀛舟)[1], and Xiumei Zhang (张秀梅)[1]

[1] School of Science, Jiangsu Provincial Research Center of Light Industrial Optoelectronic Engineering and Technology, Jiangnan University, Wuxi 214122, China
[2] School of Electronic and Information Engineering, Changshu Institute of Technology, Changshu 215556, China
[3] The 38th Research Institute of China Electronics Technology Group Corporation, Hefei 230000, China

We have fabricated the AlGaN solar-blind ultraviolet metal–semiconductor–metal (MSM) photodetectors (PDs) with an Al composition of 0.55. The surface roughness and dislocations of the high-Al-content $Al_{0.55}Ga_{0.45}N$ epitaxial layer are analyzed by atomic force microscopy and transmission electron microscopy, respectively. The device exhibits high spectral responsivity and external quantum efficiency due to the photoconductive gain effect. The current reveals a strong dependence on high temperatures in the range of 4–10 V. Moreover, the Poole–Frenkel emission model and changing space charge regions are employed to explain the carrier transport and photoconductive gain mechanisms for the AlGaN PD, respectively.

Keywords: metal–semiconductor–metal; solar blindness; photodetector; Poole–Frenkel emission; photoconductive gain.
DOI: 10.3788/COL202119.082504

1. Introduction

Ultraviolet (UV) photodetectors (PDs) have obtained wide applications in many fields due to their huge advantages, such as superior thermal stability, high sensitivity, and reliability[1–3]. AlGaN ternary materials are the optimal candidate for fabricating UV detectors compared to ZnO or Ga_2O_3 materials, because the issue of stable p-type doping for the ZnO materials needs to be overcome, and the performances of Ga_2O_3-based UV PDs are over-dependent on the crystal quality[4,5]. On the contrary, AlGaN ternary materials can tune the bandgap from 3.4 eV (360 nm) to 6.2 eV (200 nm) by adjusting the Al composition, and achieve true solar-blind (200–280 nm) detection[6,7]. Therefore, AlGaN ternary materials have been devoted to various types of solid-state UV detectors, including metal–semiconductor–metal (MSM) devices, p-n junction photodiodes, and Schottky diode detectors[8]. More importantly, MSM AlGaN-based UV PDs have attracted more attention due to fabrication simplicity, low capacitance, low dark current, and intentional doping requirements[9–11].

As is well known, MSM PD structures consist of two metal electrodes with back-to-back Schottky contact, one in positive contact and the other in reverse bias contact. The ideal MSM PDs with Schottky contact are not expected to exhibit an internal gain, and the responsivity should not change with the applied bias[12,13]. However, most of the present AlGaN-based MSM PDs exhibit high internal gain and responsivity[11,12,14]. It is believed that the reverse leakage is related to the trapping of dislocations and defects within the active layer and near the metal–semiconductor (M-S) interface, which induces persistent photoconductive effects and high photoconductive gain[12,15]. Besides, for AlGaN-based solar-blind PDs with high Al composition, structural defects like high-density threading screw dislocations occur during the actual heteroepitaxial growth process. When high-density threading screw dislocations exist in the conductive path, a high reverse leakage current will be generated in the Schottky contact[16–18]. In order to improve the performance of AlGaN-based solar-blind UV MSM PDs, it is essential to explore the carrier transport and photoconductive gain mechanisms in detail.

Here, we have fabricated an $Al_{0.55}Ga_{0.45}N$ solar-blind MSM PD. The MSM PD possesses high spectral responsivity and external quantum efficiency due to the photoconductive gain mechanism. Furthermore, the dark current and photocurrent of the PD at room and high temperatures are investigated, indicating its excellent working characteristic at high temperature. The Poole–Frenkel emission (PFE) model and changing space charge regions are explored to explain the carrier transport and photoconductive gain mechanisms for high-Al-content $Al_{0.55}Ga_{0.45}N$ solar-blind MSM PDs, respectively.
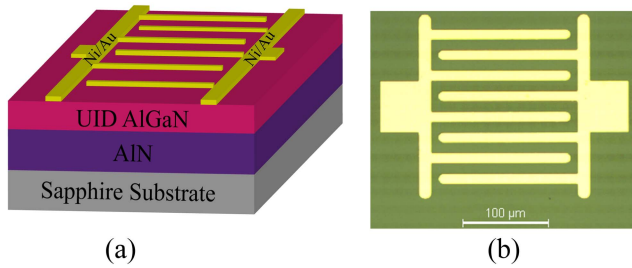
Fig. 1. (a) Epitaxial structure of the $Al_{0.55}Ga_{0.45}N$ solar-blind MSM PD. (b) Optical microscopy image of the $Al_{0.55}Ga_{0.45}N$ MSM PD with an area of 200 μm × 200 μm.

2. Experimental Details

Figure 1(a) illustrates the epitaxial structure of the $Al_{0.55}Ga_{0.45}N$ solar-blind MSM PD. The PD epitaxial layers were grown by metal organic chemical vapor deposition (MOCVD), which consisted of a sapphire substrate, a 1 μm AlN buffer layer, and a 1 μm unintentionally doped (UID) $Al_{0.55}Ga_{0.45}N$ active layer. Figure 1(b) shows an optical microscopy image of the fabricated AlGaN PD. To form two back-to-back Schottky contact electrodes, 50 nm Ni and 100 nm Au metal stacks were fabricated on the surface of the $Al_{0.55}Ga_{0.45}N$ active layer by electron beam (EB) evaporation, and eight sets of interdigital electrodes with a length of 200 μm were formed. The widths and the spacings of the interdigital electrodes were both 12 μm. The contact electrodes were annealed at 250°C for 120 s through rapid thermal annealing in a N_2 environment.

The crystal phase and morphology of the $Al_{0.55}Ga_{0.45}N$ epitaxial layer were characterized by atomic force microscopy (AFM) and high-resolution X-ray diffraction (XRD). A transmission electron microscope (TEM) was employed to analyze the dislocations of the $Al_{0.55}Ga_{0.45}N$ layer. Temperature-dependent current–voltage (*I-V*) curves were characterized by utilizing a Keithley 4200 semiconductor parameter analyzer in dark or under the illumination of 230 nm monochromatic light. The temperature was controlled from 300 K to 425 K on a probe station with a heater. In addition, the spectral responsivity of the PD was measured using a monochromator fitted with a 500 W xenon lamp as the excitation source. The optical power density at different wavelengths was calibrated by a standardized Si-based PD.

3. Results and Discussion

Figure 2(a) displays the omega-2theta XRD pattern of the $Al_{0.55}Ga_{0.45}N(002)$ plane, where the diffraction peaks of the $Al_{0.55}Ga_{0.45}N$ active layer and the AlN buffer layer can be clearly observed. A 5 μm × 5 μm AFM image of the $Al_{0.55}Ga_{0.45}N$ surface shown in Fig. 2(b) indicates that typical step-flow structures dominate the surface morphology, and the surface root-mean-square (RMS) roughness is 1.02 nm. Figures 2(c) and 2(d) show the dark-field TEM images of the $Al_{0.55}Ga_{0.45}N/AlN$ interface, where the AlGaN active layer and the AlN buffer layer
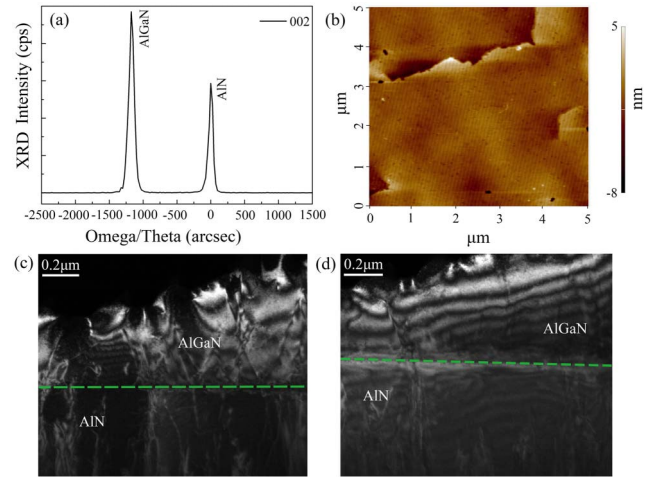

Fig. 2. (a) Omega-2theta XRD pattern of the $Al_{0.55}Ga_{0.45}N$ (002) plane. (b) Typical 5 μm × 5 μm AFM image of the AlGaN epitaxial layer. (c), (d) TEM images of the AlGaN/AlN interface.

are separated by the green dashed line. It is estimated from the TEM images that the screw dislocation density is $7.88 \times 10^8 \text{ cm}^{-2}$, and the edge dislocation density is $1.31 \times 10^9 \text{ cm}^{-2}$ for the $Al_{0.55}Ga_{0.45}N$ active layer.

Figure 3(a) shows the transmission spectrum of the $Al_{0.55}Ga_{0.45}N$ active layer. A sharp cutoff appears in the transmission spectrum curve around 265 nm with the transmittance reaching 65%, which verifies the Al content of 0.55 in the AlGaN active layer. Figure 3(b) exhibits the spectral response at different bias voltages for the $Al_{0.55}Ga_{0.45}N$ solar-blind MSM PD on a logarithmic scale. It can be seen that the responsivities under different voltages exhibit maximum peaks at about 265 nm with optical power of 6.5 μW/mm², which further corresponds to the bandgap of AlGaN with an Al content of 0.55. In addition, assuming that the gain is one, and the external quantum efficiency is 100%, the ideal responsivity expected for $Al_{0.55}Ga_{0.45}N$ MSM PD is 0.21 A/W from[19]

$$R = \frac{q\lambda}{hc}, \tag{1}$$

where *q* is the charge of an electron, *λ* is the cutoff wavelength of $Al_{0.55}Ga_{0.45}N$, and *h* is Planck's constant. It is found that the
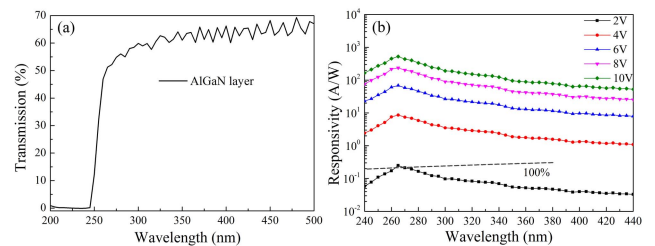

Fig. 3. (a) Transmission spectrum of $Al_{0.55}Ga_{0.45}N$ active layer. (b) Photo-response spectra of the $Al_{0.55}Ga_{0.45}N$ PD from 2 to 10 V at room temperature on the logarithmic scale.

external quantum efficiency corresponding to the maximum spectral responsivity value under a bias of 2 V is higher than 100% from Fig. 3(b). Furthermore, the external quantum efficiency corresponding to the maximum spectral responsivity at 4 V is far greater than 1000%. The UV/visible rejection ratios under different bias voltages are less than 10, which implies the presence of internal photoconductive gain characteristics in the $Al_{0.55}Ga_{0.45}N$ MSM PD[20]. This gain mechanism in the $Al_{0.55}Ga_{0.45}N$ MSM PD might be proposed by the photoconductive gain and will be explored in detail in the following part.

Figure 4 shows the I-V curves of the $Al_{0.55}Ga_{0.45}N$ PD in dark and under 230 nm UV illumination at 25°C and 150°C. It is observed that the $Al_{0.55}Ga_{0.45}N$ MSM PD has a low dark current of approximately 2.56 nA under a bias voltage of 2 V. In addition, the specific detectivity ratio ($D^\star$) under weak signals is an important indicator for evaluating the comprehensive performance of PDs and can be determined by[21,22]

$$D^\star = \frac{R}{\sqrt{2qJ_d}} = \frac{R}{\sqrt{2qI_d/A}}, \quad (2)$$

where R is the responsivity at 265 nm [shown in Fig. 3(b)], and J_d and I_d are the dark current density and dark current, respectively. A is the PD's effective illuminated area (4×10^{-8} m^2). Therefore, the calculated detectivity of the $Al_{0.55}Ga_{0.45}N$ MSM PD is 2.34×10^{10} Jones and 6.62×10^9 Jones at 25°C and 150°C under a bias voltage of 4 V, respectively, which indicates that the $Al_{0.55}Ga_{0.45}N$ solar-blind PD possesses a high ability to detect low-level incident light under high-temperature conditions. While under a bias voltage of 20 V, the $Al_{0.55}Ga_{0.45}N$ MSM PD generates a relatively high dark current of about 1×10^{-5} A. Additionally, the inset of Fig. 4 displays the breakdown characteristic of the MSM PD. The dark current rises and tends to be saturated, while the bias voltage exceeds 48.5 V, leading to the avalanche breakdown of the $Al_{0.55}Ga_{0.45}N$ MSM PD.

In order to study the carrier transport mechanism of the high-Al-content $Al_{0.55}Ga_{0.45}N$ MSM PD, the I-V characteristics measured under di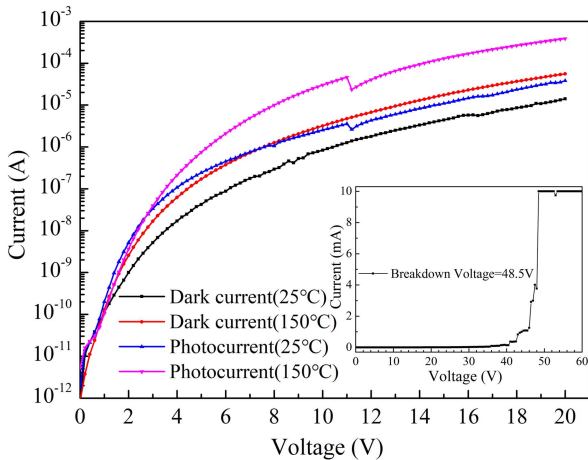fferent temperatures are depicted in Fig. 5. It is found that when the bias voltage is less than 4 V, the curves of the reverse leakage current at different temperatures basically overlap, indicating that the leakage current exhibits weak dependence on the temperature at low bias voltage, which demonstrates that the tunneling effect is the dominant origin of leakage current flow[23]. While the bias voltage exceeds 4 V, the measured macroscopic currents are observed to be obviously dependent on temperature and applied voltages. Therefore, the physical model based on the PFE is reasonable for exploring the carrier transport mechanism of the device under different temperatures and bias voltages.

It is well known that the current related to PFE is expressed as[24,25]

$$I_{PF} = CE \exp\left[-\frac{q\left(\phi_t - \sqrt{qE/\pi\varepsilon_s\varepsilon_0}\right)}{kT} \right], \quad (3)$$

or

$$\ln(I_{PF}/E) = \ln(C) - \frac{q}{kT}\phi_t + \frac{q}{kT}\sqrt{\frac{qE}{\pi\varepsilon_s\varepsilon_0}},$$

$$\equiv m(T)\sqrt{E} + n(T), \quad (4)$$

$$m(T) = \frac{q}{kT}\sqrt{\frac{q}{\pi\varepsilon_s\varepsilon_0}}, \quad (5)$$

and

$$n(T) = -\frac{q}{kT}\phi_t + \ln(C), \quad (6)$$

where E represents the electric field in the semiconductor depletion region, ϕ_t refers to the barrier height for electron emission from the trap state, and ε_s and ε_0 are the relative dielectric

Fig. 4. I-V curves of the $Al_{0.55}Ga_{0.45}N$ MSM PD in the dark and under 230 nm illumination at 25°C and 150°C. The inset is the breakdown voltage of the PD.
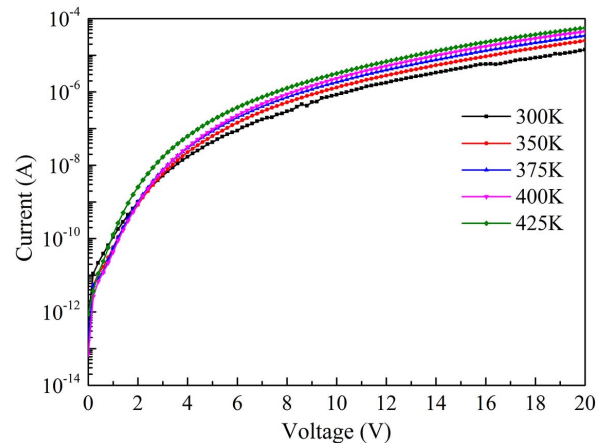

Fig. 5. Temperature-dependent I-V characteristics of the $Al_{0.55}Ga_{0.45}N$ MSM PD in dark conditions.

permittivity and permittivity of free space, respectively. k denotes the Boltzmann's constant, and T is the temperature[26]. Accordingly, if PFE is the dominant transport mechanism that causes the high dark current in the measured MSM PD device, then the measured current would increase with the increase of temperature. At a given temperature, the calculated $\ln(I_{PF}/E)$ should change linearly with $\sqrt{E}$. Figure 6(a) exhibits $\ln(I_{PF}/E)$ as a function of $\sqrt{E}$ for the I-V curves at different temperatures. All of them follow the expected linear change, which confirms that PFE is the dominant mechanism for the leakage current of the device. In addition, Figs. 6(b) and 6(c) display the $m(T)$ and $n(T)$ versus q/kT, as defined in Eqs. (5) and (6), respectively. The values of the high-frequency relative dielectric permittivity ε_s and the emission barrier height ϕ_t can be extracted from the slopes of $m(T)$ versus q/kT and the slopes of $n(T)$ versus q/kT, respectively, It is obtained that $\varepsilon_s(Al_{0.55}Ga_{0.45}N) = 5.15$ and $\phi_t = 0.08$ eV. The value of ε_s is in good agreement with the previously reported value of 4.77 for AlN and 5.35 for GaN[23,27], which further indicates the rationality of the PFE model for the leakage current transport. Moreover, the emission barrier height of 0.08 eV and Schottky barrier height of 1.55 eV are calculated at the $Ni/Al_{0.55}Ga_{0.45}N$ interface[28]. Figure 6(d) shows that the energy level of the trap state is very close to the metal Fermi level, which indicates that the leakage current is likely to be an emission of electrons from this trapped state within $Al_{0.55}Ga_{0.45}N$ into conductive dislocation under high-temperature conditions.

As discussed above, the high internal gain existing in the $Al_{0.55}Ga_{0.45}N$ MSM PD is proposed to be caused by photoconductive gain. Here, we adopted the model of space charge region change inside the semiconductor to explain the photoconductivity gain. The current responsivity R of this model can be expressed by[20]
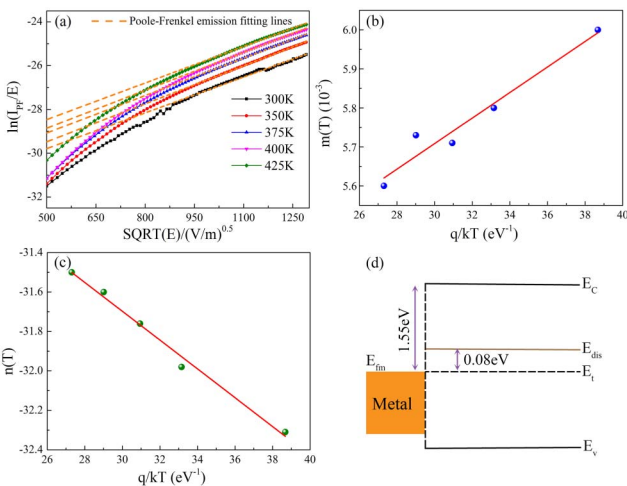

Fig. 6. (a) Derived $\ln(I_{PF}/E)$ versus sqrt(E) curves employing PFE as carrier transport mechanism at high bias voltages. (b) Derived linear fit of parameter $m(T)$ versus q/kT. (c) Linear fit of parameter $n(T)$ versus q/kT. (d) Schematic drawing of the energy band of the metal/AlGaN interface.
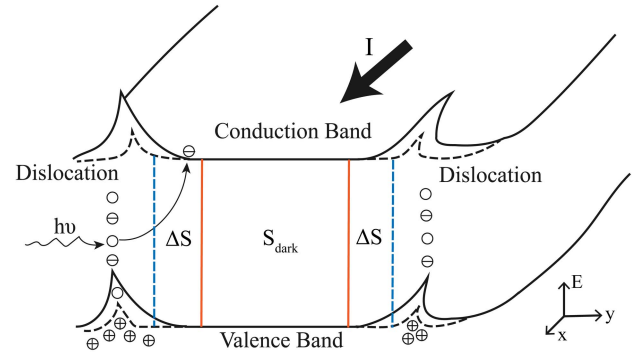

Fig. 7. Band diagram in the cross section of the AlGaN photoconductor. The dashed line represents the contraction of the band bending around the dislocation under UV illumination.

$$R = \frac{\Delta I}{P_{opt}} = \frac{qV\mu_e}{L}\left(\frac{\eta g\tau S}{hc/\lambda} + \frac{n}{P_{opt}}\Delta S\right), \quad (7)$$

where P_{opt} is the incident optical power, V is the applied bias voltage, μ_e is the electron mobility, L is the distance between the electrodes, η is the quantum efficiency, τ is the excess of free carrier lifetime, S is space charge region, and ΔS is the amount of change in the space charge region. ΔS is the dominant reason for the high photoconductivity responsivity as found by Monroy et al.[20]. Due to the high-density defects in the high-Al-content AlGaN active layer, such as screw dislocations and edge dislocations, they would trap electrons and become negatively charged, forming the depletion area around the defects, which will reduce the space charge regions (S_{dark}) of the MSM PD device. Under UV illumination, electron–hole pairs are generated in the depletion region, where a large number of holes are accumulated in the defects due to different speeds of electrons and holes. The trapped holes attract a small number of electrons, and most of the electrons move directionally under a high electric field. This would reduce the net charge near the defect and the depletion region area, which increases the space charge region (ΔS) of the corresponding AlGaN active area, as shown in Fig. 7. Thus, the photoconductive gain is believed to be dominated by the increase of the space charge region.

4. Conclusion

In conclusion, high-Al-content $Al_{0.55}Ga_{0.45}N$ solar-blind MSM PDs were fabricated, and they possess high spectral responsivity, external quantum efficiency, and low UV/visible rejection ratios. It also reveals a solar-blind photo-response with a sharp cutoff wavelength at about 265 nm, and high detectivities of 2.34×10^{10} Jones and 6.62×10^9 Jones at 25°C and 150°C under a bias voltage of 4 V are obtained. The extremely high external quantum efficiency indicates the photoconductive gain mechanism for the $Al_{0.55}Ga_{0.45}N$ MSM PDs, which is illustrated by the reduction of the depletion region and the increase in the space charge region under UV illumination. Additionally, the I-V characteristics under different voltages and temperatures

demonstrate that the carrier transport of the fabricated solar-blind PDs is dominated by the PFE mechanism.

References

1. D. Y. Guo, K. Chen, S. L. Wang, F. M. Wu, A. P. Liu, C. R. Li, P. G. Li, C. K. Tan, and W. H. Tang, "Self-powered solar-blind photodetectors based on α/β phase junction of Ga₂O₃," Phys. Rev. Appl. **13**, 024051 (2020).
2. C. H. Zeng, W. K. Lin, T. He, Y. K. Zhao, Y. H. Sun, Q. Cui, X. Zhang, S. L. Lu, X. M. Zhang, Y. M. Xu, M. Kong, and B. S. Zhang, "Ultraviolet-infrared dual-color photodetector based on vertical GaN nanowire array and graphine," Chin. Opt. Lett. **18**, 112501 (2020).
3. X. Y. Zhou, X. Tan, Y. G. Wang, X. B. Song, T. T. Han, J. Li, W. L. Lu, G. D. Gu, S. X. Liang, Y. J. Lu, and Z. H. Feng, "High-performance 4H-SiC p-i-n ultraviolet avalanche photodiodes with large active area," Chin. Opt. Lett. **17**, 090401 (2019).
4. B. Zhao, F. Wang, H. Y. Chen, Y. P. Wang, M. M. Jiang, X. S. Fang, and D. X. Zhao, "Solar-blind avalanche photodetector based on single ZnO–Ga₂O₃ core–shell microwire," Nano. Lett. **15**, 3988 (2015).
5. J. Yu, C. X. Shan, X. M. Huang, X. W. Zhang, S. P. Wang, and D. Z. Shen, "ZnO-based ultraviolet avalanche photodetectors," J. Phys. D **46**, 305105 (2013).
6. K. K. Tian, C. S. Chu, J. M. Che, H. Shao, J. Q. Kou, Y. H. Zhang, Z. H. Zhang, and T. B. Wei, "On the polarization self-screening effect in multiple quantum wells for nitride-based near ultraviolet light-emitting diodes," Chin. Opt. Lett. **17**, 122301 (2019).
7. Z. G. Shao, D. J. Chen, Y. L. Liu, H. Lu, R. Zhang, Y. D. Zheng, L. Li, and K. X. Dong, "Significant performance improvement in AlGaN solar-blind avalanche photodiodes by exploiting the built-in polarization electric field," IEEE J. Sel. Top. Quantum Electron. **20**, 3803306 (2014).
8. E. Monroy, F. Calle, J. A. Garrido, P. Youinou, E. Muñoz, F. Omnès, B. Beaumont, and P. Gibart, "Si-doped Al_xGa_{1-x}N photoconductive detectors," Semicond. Sci. Technol. **14**, 685 (1999).
9. H. Jiang, N. Nakata, G. Y. Zhao, H. Ishikawa, C. L. Shao, T. Egawa, T. Jimbo, and M. Umeno, "Back-illuminated GaN metal-semiconductor-metal UV photodetector with high internal gain," Jpn. J. Appl. Phys. **40**, L505 (2001).
10. S. Walde, M. Brendel, U. Zeimer, F. Brunner, S. Hagedorn, and M. Weyers, "Impact of open-core threading dislocations on the performance of AlGaN metal-semiconductor-metal photodetectors," J. Appl. Phys. **123**, 161551 (2018).

11. F. Xie, H. Lu, D. J. Chen, P. Han, R. Zhang, Y. D. Zheng, L. Li, W. H. Jiang, and C. Chen," Large-area solar-blind AlGaN-based MSM photodetectors with ultra-low dark current," Electron. Lett. **47**, 930 (2011).
12. O. Katz, V. Garber, B. Meyler, G. Bahir, and J. Salzman, "Gain mechanism in GaN Schottky ultraviolet detectors," Appl. Phys. Lett. **79**, 1417 (2001).
13. Y. Xu, X. H. Chen, D. Zhou, F. F. Ren, J. J. Zhou, S. Bai, H. Lu, S. Gu, R. Zhang, Y. D. Zheng, and J. D. Ye, "Carrier transport and gain mechanisms in β–Ga₂O₃-based metal–semiconductor–metal solar-blind Schottky photodetectors," IEEE Trans. Electron Devices **66**, 2276 (2019).
14. H. Srour, J. P. Salvestrini, A. Ahaitouf, S. Gautier, T. Moudakir, B. Assouar, M. Abarkan, S. Hamady, and A. Ougazzaden, "Solar blind metal-semiconductor-metal ultraviolet photodetectors using quasi-alloy of BGaN/GaN superlattices," Appl. Phys. Lett. **99**, 221101 (2011).
15. O. Katz, G. Bahir, and J. Salzman, "Persistent photocurrent and surface trapping in GaN Schottky ultraviolet detectors," Appl. Phys. Lett. **84**, 4092 (2004).
16. D. B. Li, X. J. Sun, H. Song, Z. M. Li, Y. R. Chen, G. Q. Miao, and H. Jiang, "Influence of threading dislocations on GaN-based metal-semiconductor-metal ultraviolet photodetectors," Appl. Phys. Lett. **98**, 1541 (2011).
17. P. K. Rao, B. Park, S. T. Lee, Y. K. Noh, M. D. Kim, and J. E. Oh, "Analysis of leakage current mechanisms in Pt/Au Schottky contact on Ga-polarity GaN by Frenkel–Poole emission and deep level studies," J. Appl. Phys. **110**, 013716 (2011).
18. B. S. Simpkins, E. T. Yu, P. Waltereit, and J. S. Speck, "Correlated scanning Kelvin probe and conductive atomic force microscopy studies of dislocations in gallium nitride," J. Appl. Phys. **94**, 1448 (2003).
19. S. Rathkanthiwar, A. Kalra, S. V. Solanke, N. Mohta, R. Muralidharan, S. Raghavan, and D. N. Nath, "Gain mechanism and carrier transport in high responsivity AlGaN-based solar blind metal semiconductor metal photodetectors," J. Appl. Phys. **121**, 164502 (2017).
20. E. Monroy, F. Calle, E. Munoz, F. Omnès, B. Beaumont, and P. Gibart, "Visible-blindness in photoconductive and photovoltaic AlGaN ultraviolet detectors," J. Electron. Mater. **28**, 240 (1999).
21. N. Youngblood, C. Chen, S. J. Koester, and M. Li, "Waveguide-integrated black phosphorus photodetector with high responsivity and low dark current," Nat. Photon. **9**, 247 (2015).
22. X. K. Zhou, D. Z. Yang, D. G. Ma, A. Vadim, T. Ahamad, and S. M. Alshehri, "Ultrahigh gain polymer photodetectors with spectral response from UV to near-infrared using ZnO nanoparticles as anode interfacial layer," Adv. Funct. Mater. **26**, 6619 (2016).
23. H. Zhang, E. J. Miller, and E. T. Yu, "Analysis of leakage current mechanisms in Schottky contacts to GaN and Al₀.₂₅Ga₀.₇₅N/GaN grown by molecular-beam epitaxy," J. Appl. Phys. **99**, 023703 (2006).
24. F. C. Chiu, "A review on conduction mechanisms in dielectric films," Adv. Mater. Sci. Eng. **2014**, 578168 (2014).
25. E. Arslan, S. Buetuen, and E. Ozbay, "Leakage current by Frenkel–Poole emission in Ni/Au Schottky contacts on Al₀.₈₃In₀.₁₇N/AlN/GaN heterostructures," Appl. Phy. Lett. **94**, 142106 (2009).
26. J. R. Yeargan and H. L. Taylor, "The Poole–Frenkel effect with compensation present," J. Appl. Phys. **39**, 5600 (1968).
27. V. W. L. Chin, T. L. Tansley, and T. Osotchan, "Electron mobilities in gallium, indium, and aluminum nitrides," J. Appl. Phys. **75**, 7365 (1994).
28. O. Ambacher, J. Majewski, C. Miskys, A. Link, M. Hermann, M. Eickhoff, M. Stutzmann, F. Bernardini, V. Fiorentini, and V. Tilak, "Pyroelectric properties of Al(In)GaN/GaN hetero- and quantum well structures," J. Phys. Condens. Matter **14**, 3399 (2002).